

AD-A073 716 AIR FORCE GEOPHYSICS LAB HANSCOM AFB MA  
AIRBORNE ALL-SKY IMAGING OF EQUATORIAL AIRGLOW.(U)  
SEP 78 E J WEBER, J BUCHAU, J G MOORE

F/G 4/1

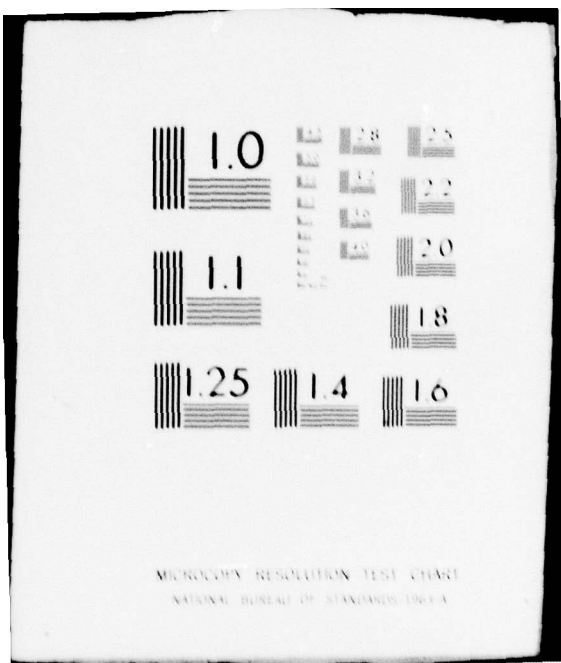
UNCLASSIFIED

AFGL-TR-78-0224

NL

| OF |  
AD  
A073716

END  
DATE  
FILMED  
10-79  
DDC



MICROSCOPY RESOLUTION TEST CHART  
NATIONAL BUREAU OF STANDARDS 1953 A

ADA 073716

AFGL-TR-78-0224  
ENVIRONMENTAL RESEARCH PAPERS, NO. 641



## Airborne All-Sky Imaging of Equatorial Airglow

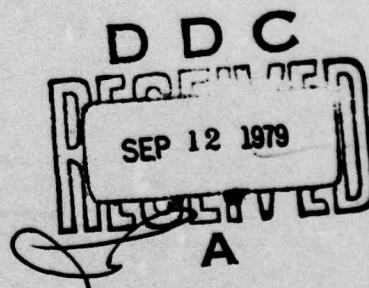
E. J. WEBER, Capt, USAF  
J. BUCHAU  
J. G. MOORE

21 September 1978

This research was sponsored, in part, by the Air Force Laboratory Independent Research Fund.

This research was sponsored in part by the Defense Nuclear Agency (DNA) under subtask I25AAXHX633, Work Unit 33 entitled "Communications Effects Data Base."

Approved for public release; distribution unlimited.



SPACE PHYSICS DIVISION PROJECT 4643  
AIR FORCE GEOPHYSICS LABORATORY  
HANSCOM AFB, MASSACHUSETTS 01731

AIR FORCE SYSTEMS COMMAND, USAF

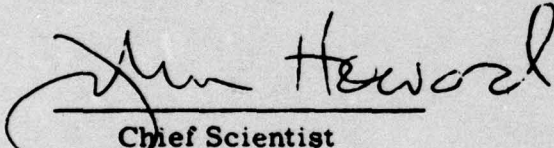


79 09 12 042

This report has been reviewed by the ESD Information Office (OI) and is  
releasable to the National Technical Information Service (NTIS).

This technical report has been reviewed and  
is approved for publication.

FOR THE COMMANDER

  
John Howard  
Chief Scientist

Qualified requestors may obtain additional copies from the  
Defense Documentation Center. All others should apply to the  
National Technical Information Service.

(14) AFGL-TR-78-0204  
AFGL-ERP-641

Unclassified

SECURITY CLASSIFICATION OF THIS PAGE (When Data Entered)

REPORT DOCUMENTATION PAGE		READ INSTRUCTIONS BEFORE COMPLETING FORM
1. REPORT NUMBER  AFGL-TR-78-0224	2. GOVT ACCESSION NO.	3. RECIPIENT'S CATALOG NUMBER  (9)
4. TITLE (and Subtitle)  AIRBORNE ALL-SKY IMAGING OF EQUATORIAL AIRGLOW		5. TYPE OF REPORT & PERIOD COVERED  Scientific. Final Preprint
6. PERFORMING ORG. REPORT NUMBER  Air Force Geophysics Laboratory (PHI)		7. CONTRACT OR GRANT NUMBER(s)  ERP No. 641
8. PERFORMING ORGANIZATION NAME AND ADDRESS  Air Force Geophysics Laboratory (PHI) Hanscom AFB Massachusetts 01731		10. PROGRAM ELEMENT, PROJECT, TASK AREA & WORK UNIT NUMBERS  62101F 46430504 (11)05
11. CONTROLLING OFFICE NAME AND ADDRESS  Air Force Geophysics Laboratory (PHI) Hanscom AFB Massachusetts 01731		12. REPORT DATE  21 September 1978
13. MONITORING AGENCY NAME & ADDRESS (if different from Controlling Office)		14. NUMBER OF PAGES  45
		15. SECURITY CLASS. (of this report)  Unclassified
		15a. DECLASSIFICATION/DOWNGRADING SCHEDULE
16. DISTRIBUTION STATEMENT (of this Report)  Approved for public release; distribution unlimited.		
17. DISTRIBUTION STATEMENT (of the abstract entered in Block 20, if different from Report)		
18. SUPPLEMENTARY NOTES This research was sponsored, in part, by the Air Force Laboratory Independent Research Fund.  This research was sponsored in part by the Defense Nuclear Agency (DNA) under subtask I25AAHX633, Work Unit 33, entitled "Communications Effects Data Base."		
19. KEY WORDS (Continue on reverse side if necessary and identify by block number)  Ionospheric irregularities All sky imaging photometer Equatorial airglow Equatorial spread F		
20. ABSTRACT (Continue on reverse side if necessary and identify by block number)  Radio wave and optical experiments were conducted in March 1977 and March 1978 at low magnetic latitudes to investigate the effects of F region electron density irregularities on transionospheric communications links. Imaging photometer, ionosonde, 50 MHz backscatter radar and satellite amplitude scintillation measurements were used to arrive at a description of equatorial F-region disturbances. After sunset, regions of low electron density propagate from the bottomside, through the F-region peak and often reach to		

DD FORM 1 JAN 73 1473 EDITION OF 1 NOV 65 IS OBSOLETE

Unclassified

SECURITY CLASSIFICATION OF THIS PAGE (When Data Entered)

409 578

79 09 12 042

703

Unclassified

SECURITY CLASSIFICATION OF THIS PAGE(When Data Entered)

**20. Abstract (Continued)**

1000 km altitude. These regions of low density, called bubbles or plumes, are visible as depletions in the 6300 Å OI airglow; therefore, the size and motion of these depletions can be measured with an all sky imaging photometer. Electron density irregularities, with scale sizes from 3 m to 10 km, are found within these plumes, and give rise to amplitude scintillation, 50 MHz back-scatter and spread F. This report presents a review of the experimental measurements used to arrive at the current description of equatorial F region plumes and associated irregularities.

Unclassified

SECURITY CLASSIFICATION OF THIS PAGE(When Data Entered)

## Preface

We thank the following members of the Air Force Geophysics Laboratory for their contributions: Dr. J. Aarons and Lt Col A. L. Snyder for their support of and interest in the scintillation research program; R. W. Gowell, J. B. Waaramaa and J. W. F. Lloyd for the engineering and flying support of the airborne missions; R. Carnevale for providing logistics support; MSgt G. A. Coolidge and A1C P.J. Diroll for the enthusiastic support of the all-sky photometer data analysis. We thank Dr. R. H. Eather for assistance with the all-sky photometer, the personnel of the Jicamarca Radio Observatory for taking and processing the radar information and Dr. J. P. McClure for providing the radar maps. The strong support from the air and ground crews of the 4950th Test Wing, Wright-Patterson AFB, Ohio, made it possible to achieve the goals of this program.

This research was sponsored, in part, by the Air Force Laboratory Independent Research Fund of the Air Force Geophysics Laboratory, Air Force Systems Command and, in part, by the Defense Nuclear Agency under Subtask Code 125AAXHX633, Work Unit 33.

Accession For	
NTIS GRA&I	<input checked="" type="checkbox"/>
DDC TAB	<input type="checkbox"/>
Unannounced	<input type="checkbox"/>
Justification	<input type="checkbox"/>
By _____	
Distribution/	
Availability Codes	
Dist.	Avail and/or special
A	

## **Contents**

1. INTRODUCTION	7
2. ALL-SKY IMAGING PHOTOMETER	9
3. RELATION OF ISOLATED AIRGLOW DEPLETION TO IONOSPHERIC IRREGULARITIES	13
3.1 Airglow	13
3.2 Ionosonde	15
3.3 VHF Backscatter Radar	16
4. MULTIPLE STRUCTURES	18
5. AIRGLOW DEPLETIONS AT ASCENSION ISLAND	20
6. ELECTRON DENSITY ESTIMATES FROM AIRGLOW MEASUREMENTS	26
7. NORTH-SOUTH SYMMETRY	30
8. SUMMARY AND DISCUSSION	34
REFERENCES	37

## **Illustrations**

1. All Sky Imaging Photometer Optics Schematic	9
2. All Sky Imaging Photometer System Block Diagram	11

## Illustrations

3. Example of an All Sky Photometer Airglow Image Showing a North-south Aligned Depletion	14
4. All Sky ( $155^{\circ}$ Field of View) $6300 \text{ \AA OI}$ Airglow Images at 15 min Intervals From 0100 to 0545 UT, 17 March 1977	15
5. Model of an Eastward Drifting Bottomside Ne Depletion or Corrugation Based on Observed Ionosonde and Airglow Parameters	16
6. Range-time-intensity Map of Isolated F-region Disturbance Passing Over the Jicamarca 50 MHz Radar	17
7. $6300 \text{ \AA}$ All Sky Photometer Image at 0445 UT, 20 March 1977 With Four Well-developed Airglow Depletions	19
8. Ground Projection of the East and West Edges of Airglow Depletions Observed During the Flight of 20 March 1977 to Illustrate the Eastward Drift, and the F-layer Virtual Height Changes Associated With the Depletions	20
9. All Sky $6300 \text{ \AA OI}$ Airglow Images at 10 min Intervals From 2020 to 0140 UT, 10/11 March 1978	22
10. Ground Track for the Flight of 10/11 March 1978	23
11. Ground Projection of the East and West Edges of Airglow Depletions Observed During the Flight of 10/11 March 1978, and the 250 MHz Scintillation Index Measured on the Aircraft	25
12. Ground Projection of the Airglow Depletions, $6300 \text{ \AA}$ Zenith Intensity, F-layer Virtual Height and Calculated Average Bottomside Electron Density For the Flight of 20 March 1977	28
13. Ground Projection of the Airglow Depletions, $6300 \text{ \AA}$ Zenith Intensity, F-layer Virtual Height and Calculated Average Bottomside Electron Density For the Flight of 10 and 11 March 1978	29
14. $6300 \text{ \AA}$ Airglow Images North and South of the Magnetic Equator on 12 March 1978	31
15. Virtual Range vs. Time Plots at Selected Frequencies to Show Range Changes Associated With Electron Density Depletions	33

## Table

1. Summary of System Specifications	12
-------------------------------------	----

## **Airborne All-Sky Imaging of Equatorial Airglow**

### **1. INTRODUCTION**

An all-sky imaging photometer has been developed and installed in the Air Force Geophysics Laboratory's Airborne Ionospheric Observatory to monitor auroral and airglow spectral emission features. The imaging system overcomes many of the limitations associated with conventional photometric instrumentation by combining adequate spectral, spatial and temporal resolution with sufficient sensitivity to measure low-intensity emissions. In addition, the airborne capability achieved with the Airborne Ionospheric Observatory provides complementary geophysical measurements (ionosonde, scanning photometer, spectrometer, all-sky camera and VHF/UHF satellite receivers), ensures good visibility and allows access to remote geographical areas.

Airborne expeditions were conducted in March 1977 and March 1978 at equatorial latitudes to investigate the characteristics of large-scale F-region irregularities. The primary purpose of these expeditions was to relate specific features of the equatorial ionosphere to the occurrence of amplitude fluctuations (scintillations) on satellite-to-ground and satellite-to-aircraft VHF and UHF transmissions. Optical imaging measurements were performed with the objective of identifying

---

(Received for publication 21 September 1978)

airglow structures which are associated with F-region (electron density) irregularities, and to determine ionospheric conditions in the vicinity of a transionospheric 250 MHz signal ray path. These measurements showed the existence of north-south aligned depletions or regions of decreased intensity in the 6300 Å and 5577 Å OI airglow.

Initial results from measurements within a few degrees of the magnetic equator (Weber et al)<sup>1</sup> show that these depletions have east-west dimensions ranging from 50 to 200 km, with fine structure as small as 2.5 km (instrumental resolution at 250 km altitude) and often extend greater than 1200 km north-south. The depletions appear after sunset and drift toward the east with speeds of 50-150 m/s during the local evening hours. Simultaneous ionosonde measurements showed that the depletions are accompanied by strong spread F, and are characterized by an increase in the virtual height of the F-layer ( $h'F$ ). The airglow and ionosonde measurements resulted in a description of these depletions as corrugations or height variations in the bottomside of the F-layer.

Buchau et al<sup>2</sup> have shown, for one example, that airglow depletions are the optical signature of 3 m ionospheric irregularities, or plumes, measured by the Jicamarca 50 MHz backscatter radar. These plumes are thought to result from the development and upward propagation of low density bubbles in the equatorial F-region (Woodman and La Hoz<sup>3</sup>). The relation of airglow depletions to amplitude scintillations on transionospheric communication links has been examined by Buchau et al.<sup>4</sup> Passage of an airglow depletion through the signal ray path produces intense amplitude scintillation (often >20 dB at 250 MHz), and this implies the existence of kilometer size irregularities within the depletions.

A unified description of these equatorial disturbances has emerged from the combination of photometer, ionosonde, 50 MHz backscatter and scintillation measurements. The airglow depletions are the optical signatures of regions of low density, upward drifting plasma in the nighttime equatorial ionosphere. The region is confined in the east-west direction to widths of 50 to 200 km, but extends along entire magnetic flux tubes in the north-south direction. Within these regions,

1. Weber, E.J., Buchau, J., Eather, R.H., and Mende, S.B. (1978) North-south aligned equatorial airglow depletions, J. Geophys. Res. 83:712.
2. Buchau, J., Weber, E.J., and McClure, J.P. (1978a) Radio and optical diagnostics applied to an isolated equatorial scintillation event, Proc. Ionospheric Effects Symp., Arlington, VA.
3. Woodman, R.F., and LaHoz, C. (1976) Radar observations of F-region equatorial irregularities, J. Geophys. Res. 81:5447.
4. Buchau, J., Weber, E.J., and Whitney, H.E. (1978b) New insight into ionospheric irregularities and associated VHF/UHF scintillations. Proc. AGARD Conf., Digital Communications in Avionics, Munich, Germany.

ionospheric irregularities with scale sizes from 3 m to 10 km give rise to 50 MHz backscatter, scintillations and spread F. This paper will present a review of the various ionospheric measurements conducted in March 1977 and March 1978 which were used to arrive at the current description of equatorial ionospheric depletions.

## 2. ALL-SKY IMAGING PHOTOMETER

An all-sky imaging system, similar to one for ground-based observations (Mende et al)<sup>5</sup> was developed for airborne operation. The optics (Figure 1) employ a 155° field of view and are telecentric in design, ensuring the same size light cone at focal plane for each point in the field of view, thus allowing narrowband interference filters to be used. At full aperture of f1.4, 25 Å filters can be used. Four such filters mounted on a filter wheel allow sequential measurements for the most important airglow emissions.

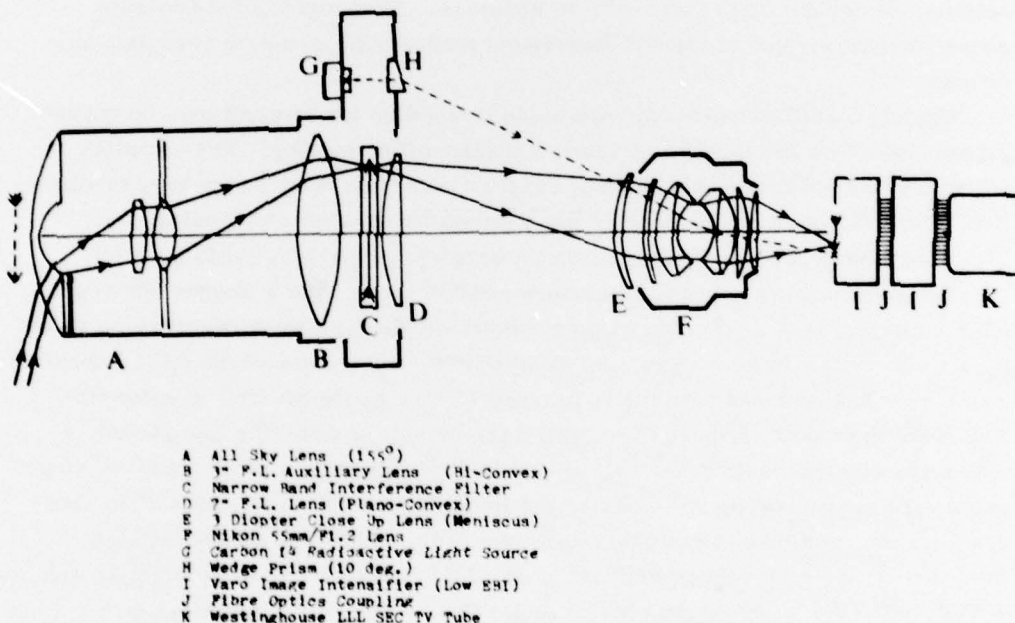


Figure 1. All Sky Imaging Photometer Optics Schematic

5. Mende, S. B., Eather, R. H., and Aamodt, E. K. (1977) Instrument for the monochromatic observation of all sky auroral images, Appl. Opt. 16:1691.

The airglow field is then re-imaged onto the faceplate of a two-stage image intensifier that is fiber-optically coupled to a low light level SEC (Secondary Emission Conductivity) TV tube. This is a charge-integrating tube that allows for time exposures of up to 3 sec at room temperature.

Sequential pictures at different wavelengths are recorded on a time-lapse video tape recorder (see system block diagram in Figure 2) and temporarily stored on a multi-track video disc that is used to drive four black and white TV monitors and a red-green-blue (RGB) color monitor that continuously display the last picture taken through each filter. These pictures are continually updated as the filter wheel rotates through the four-filter sequence.

An absolute intensity reference is supplied by a  $C^{14}$  radioactive light source that is imaged on the corner of each frame. Date, time, and filtering information is binary encoded on each picture, and date and time are also presented numerically on each picture.

The time and control sequencing for the instrument is provided by a fully programmable, special-purpose sequencer that controls the mechanical operation, exposure time, high voltage appropriate for each filter, distribution of video signals to appropriate discs, and camera exposure. Preprogrammed exposure sequences allow rapid change of operational modes appropriate to changing conditions.

Certain modifications have been made to the disc for aircraft use, to ensure proper operation and to prevent damage at take-off or landing. The complete instrument has been shock mounted, and the record/playback heads have mechanical lifters that remove the heads from the disc for take off and landing.

A summary of system operational parameters is given in Table 1.

For measurement of the low latitude airglow, four  $6300\text{ \AA}$  images and two  $5577\text{ \AA}$  images were made each minute. Both wavelengths were recorded on video tape. The  $6300\text{ \AA}$  images were also used to drive the red gun of the RGB monitor which was photographed with the time lapse 16 mm movie camera on color film. The resulting movie format proved extremely useful in detecting fine structure within the airglow images, as well as displaying drift motion of the airglow structures. To maximize signal to noise, the images were all made with a 2 sec integration time, and tube high voltage was adjusted to achieve properly exposed images. At the high voltage settings used, the dynamic range of the images was  $\sim 25$  to  $250\text{ R}$  for weak airglow levels and  $\sim 60$  to  $600\text{ R}$  for bright airglow.

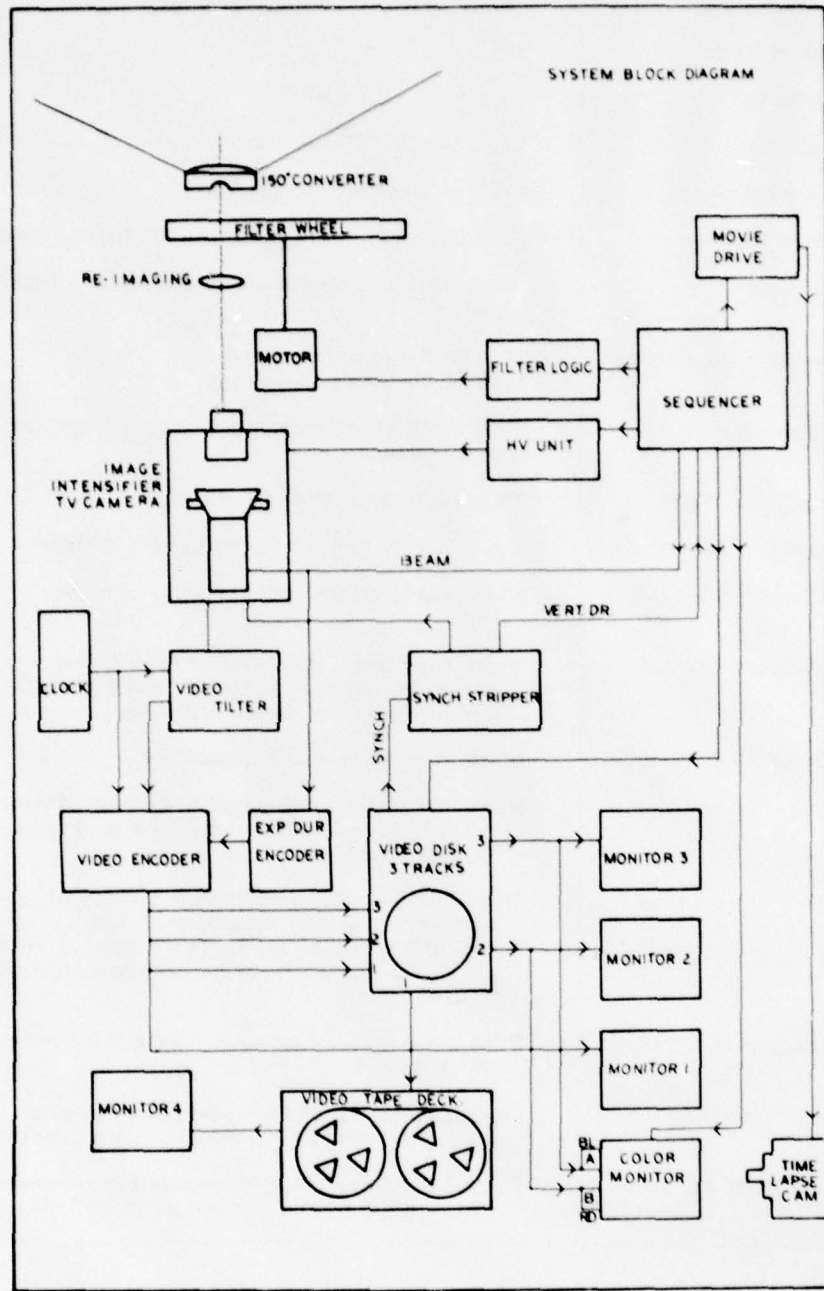


Figure 2. All Sky Imaging Photometer System Block Diagram

Table 1. Summary of System Specifications

Field of View	155°
Pass Band	25 Å at f1.4; 5 Å at f8
Resolution	1/2° zenith, 2° horizon
Spectral Response	S-20, exceeding 100 μA/lumen
Picture Storage	No detectable degradation for up to 3 seconds
Tube Gain	Photon noise granularity visible above tube noise
Threshold Sensitivity	20 R at 2 sec exposure 1 kR at 30 frames/sec
Dynamic Range	20 R to 10 kR covered by 3 preset High Voltage settings
Flatness of Field	30 percent loss at edge of field
Repetition Rate	Typically 20 sec for complete filter cycle
Temporary Storage	Video disc, three video tracks, one sync track
Permanent Storage	Video tape deck, time-lapse type (9 hour recording time on a single reel); 16 mm and 35 mm time-lapse cameras
Process Controller	In-field programming capability
Display Systems	Four black and white monitors, 9 in. diagonal; color monitor, RGB and A minus B input, 12 in. diagonal
Real-Time Display	Simultaneous fully registered display of three filter channels. Capability of displaying the difference of any two pictures. Display of two or three filters as pseudo-color on RGB monitor
Character Generators	Date/time display on each frame for frame identification
Digital Encoding	Digital encoding of time and housekeeping data for computer-controlled data handling
Flight Heading	Digital display of flight heading for recording (three digit BCD TTL compatible)

### **3. RELATION OF ISOLATED AIRGLOW DEPLETION TO IONOSPHERIC IRREGULARITIES**

#### **3.1 Airglow**

In addition to the large scale "intertropical arcs" observed by Barbier at low latitudes in the African sector (Barbier,<sup>6</sup> and Barbier et al<sup>7</sup>), medium scale airglow structures have also been investigated for many years. Steiger<sup>8</sup> and Van Zandt and Peterson<sup>9</sup> measured localized enhancements in the 6300 Å OI airglow which take the form of patches, east-west arcs and north-south ridges. These measurements were made with conventional filter photometers performing azimuth scans at several zenith angles. A map of airglow intensity contours is produced by combining all of the scans for an assumed emission height. Because of the large amount of data required to produce a detailed contour map using this technique, practical considerations limit the zenith angle increments (spatial resolution) to increase the temporal resolution. The measurements of Van Zandt and Peterson<sup>9</sup> achieved ~ 150 km (radial) resolution (at 250 km altitude) with successive 6300 Å maps separated by 15 min. While this resolution is sufficient to map large scale structures in the night airglow, it is insufficient for a detailed description of medium scale structures and drifts. The all-sky imaging photometer used in the present study overcomes these resolution limitations. Figure 3 is an example of a 6300 Å airglow image (photographed from the tape-recorded video frame) using a 2 sec integration time. The grid lines are magnetic meridians at 1° increments for an assumed emission height of 250 km. Care must be exercised in the interpretation of features near the edge of the field of view. Although the van Rhijn effect tends to increase the apparent airglow intensity at large zenith angles (a factor of 2.7 for 75° zenith angle at 250 km emission height), the wide angle lens suffers serious vignetting toward the edge of the field of view (a factor of 3.3) (Mende et al<sup>5</sup>). The two effects act in opposition, but vignetting exceeds van Rhijn enhancement at the edges, often resulting in a perceptible dark band around the image for the weak airglow features under consideration. The narrow north-south striations about 1/2° west of zenith are the three wires of the ionosonde antenna which stretch above the all-sky lens. Bright airglow fills the portion of

6. Barbier, D. (1961) Les variations d'intensité la raie 6300 Å la luminescence nocturne, Ann. Geophys. 17:5.
7. Barbier, D., Weill, G., and Glaume, J. (1961) L'émission de la raie rouge du ciel nocturne en Afrique, Ann. Geophys. 17:305.
8. Steiger, W. R. (1967) Low Latitude Observations of Airglow, in Aurora and Airglow, edited by B. M. McCormac, p. 419, Reinhold, New York.
9. Van Zandt, T. E., and Peterson, V. L. (1968) Detailed maps of tropical 6300 Å nightglow enhancements and their implications on the ionospheric F2 layer, Ann. Geophys. 24:747.

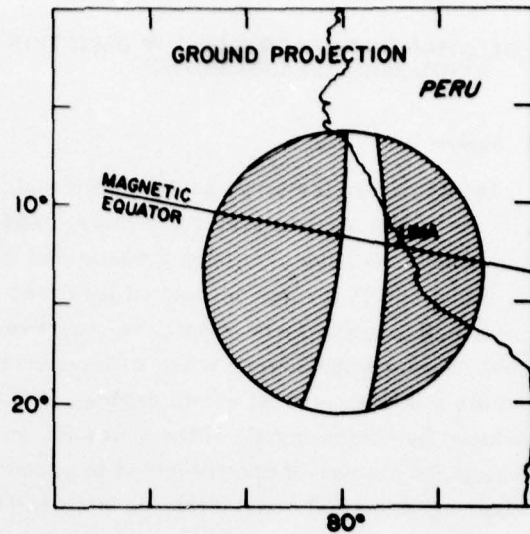
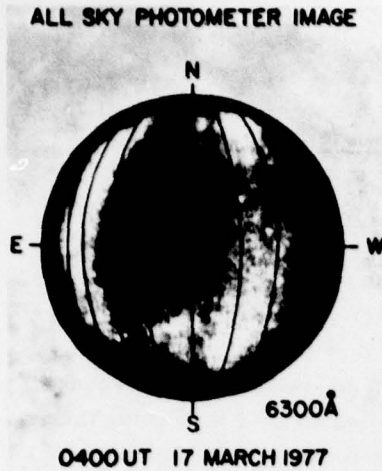


**Figure 3.** Example of an All Sky Photometer Airglow Image Showing a North-south Aligned Depletion. The grid lines are magnetic meridians at  $1^{\circ}$  intervals. The ground projection, assuming 250 km emission height is also shown

the sky from overhead to the western horizon and from  $2^{\circ}$  east of the aircraft zenith to the eastern horizon. Several stars are also visible in the image. The dark north-south band or airglow depletion between the two bright regions is a phenomenon which was routinely observed at low latitudes and is a result of decreased ionization below  $\sim 300$  km. The ground projection on the right side of Figure 3 gives an indication of the size of the field of view and the orientation and dimensions of the airglow depletion, about 165 km east-west and 1200 km north-south.

The airglow depletion shown in Figure 3 drifted from west to east across the entire 1200 km field of view of the imaging system. This motion is evident in Figure 4 which shows airglow images for the flight period in 15 min intervals. This flight consisted of a series of short north-south legs along a magnetic meridian 300 km west of Lima, Peru. All images have been reoriented with magnetic north at the top, and east to the left. The images between 0100 and 0200 UT show a low-level, unstructured glow ( $\sim 60R$ ) with some enhancement to the south due to increased emission from the equatorial edge of the Appleton anomaly. The Milky Way is visible in the 0100 to 0145 UT images as a slight enhancement aligned in the SE-NW direction. The airglow depletion is visible on the western horizon as early as 0200 UT. During the next 150 min, the depletion drifts toward the east at  $\sim 92$  m/sec and leaves the field of view by 0445 UT. When directly overhead

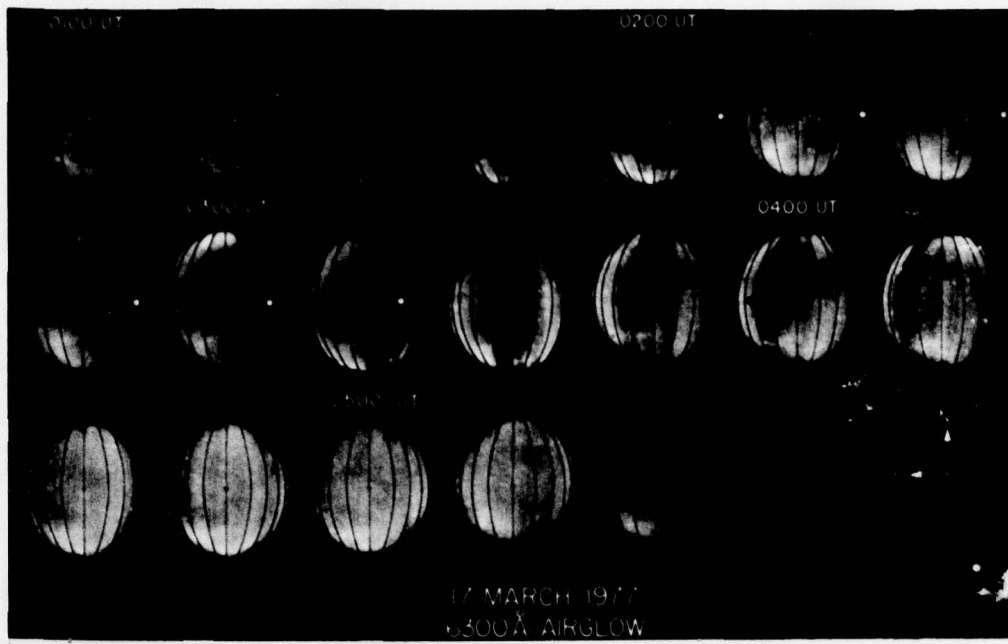


Figure 4. All Sky ( $155^{\circ}$  Field of View)  $6300 \text{ \AA}$  OI Airglow Images at 15 min Intervals From 0100 to 0545 UT, 17 March 1977. The grid indicates the projection of magnetic longitudes, at  $1^{\circ}$  intervals, for an assumed emission height of 250 km. The black and white dots represent the location of approaching and receding oblique F-region ionosonde backscatter returns, respectively

at 0330 UT the depletion is 165 km wide. Generally, the eastern or leading edge of the depletion is closely aligned along a magnetic meridian. The subject of alignment will be considered further in Section 5.

### 3.2 Ionosonde

Simultaneous measurements from the aircraft ionosonde help define the bottom-side ionospheric (electron density) structure responsible for the airglow depletion. Figure 5 shows the virtual range of overhead and oblique F-layer echoes for the period of interest.

The range changes of the oblique echoes suggest the approach and recession of scattering fronts associated with the airglow depletion. For comparison, the estimated location of the scatterers, determined from the measured range to the oblique echoes, assuming a height of 250 km are indicated as dots on the airglow image in Figure 4. The white dots indicate range to approaching echoes and the black dots indicate the receding echoes. This comparison shows that the approaching echo is associated with the trailing (western) edge of the airglow depletion while

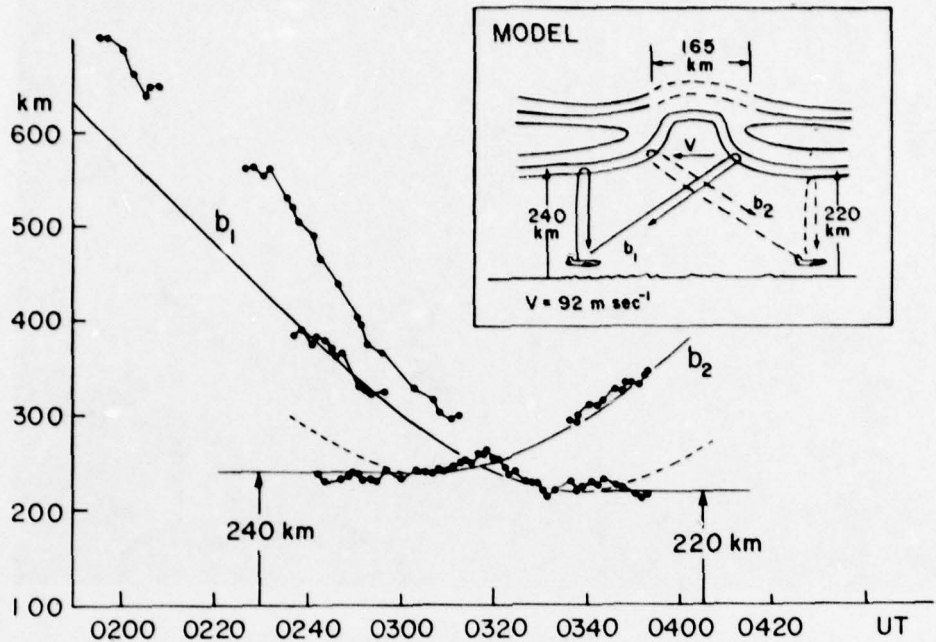


Figure 5. Model of an Eastward Drifting Bottomside Ne Depletion or Corrugation Based on Observed Ionosonde and Airglow Parameters. The measured ranges of oblique returns and the virtual height of the overhead F-region are compared with range-height changes expected from the passage of the model bottomside structure over the ionosonde

the receding echo is associated with the leading (eastern) edge. A simple bottomside model, also shown in Figure 5, has been postulated to explain the airglow depletion and the observed ionosonde returns. A bottomside electron density depletion, having the same width and drift velocity as the airglow depletion, would produce oblique echoes, using geometric considerations only, via ray paths  $b_1$  and  $b_2$ . The ranges to oblique and overhead echoes via ray paths  $b_1$  and  $b_2$  are shown as solid lines in the lower part of Figure 5 for the assumed model. Comparison with the data shows good agreement, considering the uncertainty of the actual ray paths.

### 3.3 VHF Backscatter Radar

The 50 MHz Jicamarca Backscatter Radar, in Peru, was operated during the aircraft flight to determine the relationship between F-region irregularities measured by the radar, airglow depletions, and amplitude fluctuations on satellite signals.

The 50 MHz radar has been used to study the equatorial ionosphere for several years. Of direct interest to the present studies are observation of "plumes" or low electron density bubbles which develop after sunset in the lower F region and subsequently propagate upward, sometimes reaching 1000 km altitude (Woodman and La Hoz<sup>3</sup>). The strong backscatter echoes which result from these plumes indicate the presence of ionospheric irregularities with three meter scale size.

The 50 MHz backscatter range-time-intensity plot (Figure 6, Buchau et al<sup>2</sup>) shows the time history of the development or drift of 3 m irregularities above Jicamarca. The figure can be interpreted either as the time history of an eastward drifting irregularity region observed from a fixed location or, assuming a rigid ionosphere, as an east-west cross section of such a region.

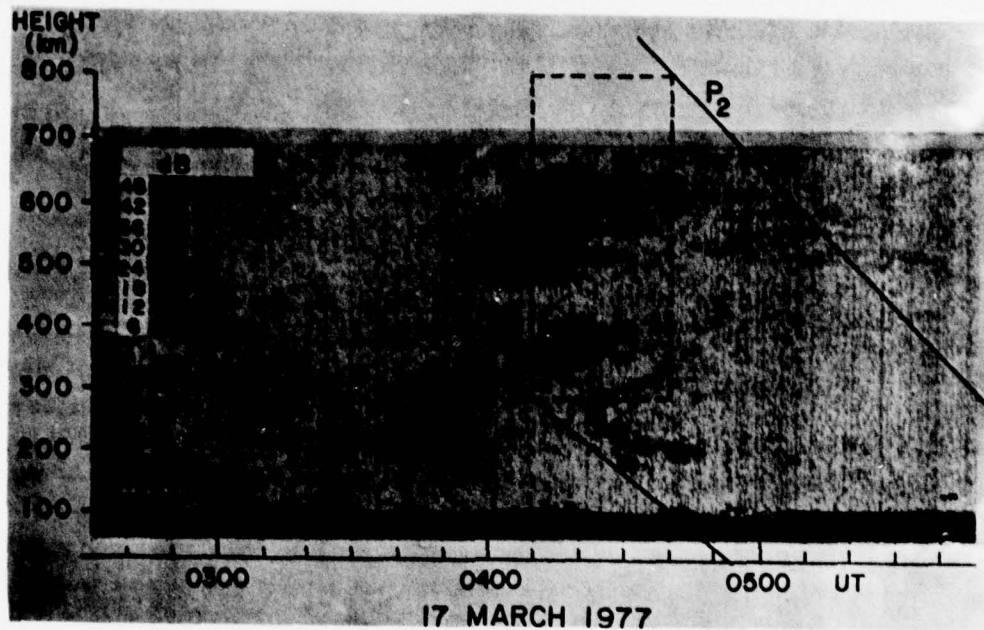


Figure 6. Range-time-intensity Map of Isolated F-region Disturbance Passing Over the Jicamarca 50 MHz radar. The dashed lines represent the irregularity cross section determined from airglow and scintillation measurements.  $P_1$  and  $P_2$  denote the transionospheric ray path through the disturbed region at the beginning and end of the associated scintillation event (from Buchau et al<sup>2</sup>)

Some irregularities are seen in the lower F-region from the beginning of the observations until 0300 UT. Starting at 0357 UT the first echoes from an extended region of irregularities are observed at 500 to 600 km height. This disturbance eventually involves the whole F-region between 175 and 670 km. Irregularities in the F-region below 500 km disappear between 0430 UT (500 km level) and 0450 UT (200 km level), while some very weak irregularities above 500 km are observed until 0535 UT. The relatively uniform diffuse background appearing at the first digital level (0 to 6 dB above threshold) was caused by a computer malfunction, and does not indicate the existence of a diffuse background of weak irregularities.

To assess the relation between the airglow depletion, the backscatter echoes and ionospheric irregularities which cause amplitude scintillation, the two dimensional cross section derived from airglow and scintillation measurements is superposed on Figure 6. The arrival time of the airglow depletion at the Jicamarca meridian is 0410 UT. At a velocity of 92 m/sec, the 165 km wide airglow depletion passed over Jicamarca in exactly 30 min. This determines the horizontal extent of the cross section shown in Figure 6. Using appropriate elevation angles for a ray path to the LES 9 geostationary satellite, ( $P_1$  and  $P_2$ ), the ray paths at the onset and end times of the observed amplitude scintillations determine the altitude limits of irregularities within the ionospheric cross section. This occurs because the eastward drift of the irregularity region effectively moves the ray path from lower to higher altitudes through this region. As the figure shows, the estimated volume is in general agreement with the observed backscatter cloud. There is a discrepancy between the shape of the simple cross section based on airglow and scintillation observations and the envelope of 3 m irregularities shown in the figure. In this example, 3 m irregularities extend over a larger east-west distance than is reflected in the airglow dimension, and over a smaller height range than suggested by the scintillation measurements.

From the combined airglow, ionosonde, 50 MHz backscatter and scintillation measurements for the isolated airglow depletion of 17 March 1977, Buchau et al<sup>2</sup> concluded that all of these measurements are different aspects of the same phenomenon, a volume of reduced electron density, containing meter to kilometer sized irregularities, extending throughout the entire F-region causing scintillation on ray paths which intersected this volume.

#### 4. MULTIPLE STRUCTURES

In addition to the isolated airglow depletions, multiple depletions have also been observed with the all-sky imaging photometer. Figure 7 shows an example of four depletions existing simultaneously within  $6^{\circ}$  of longitude, at 0445 UT, 20 March 1977

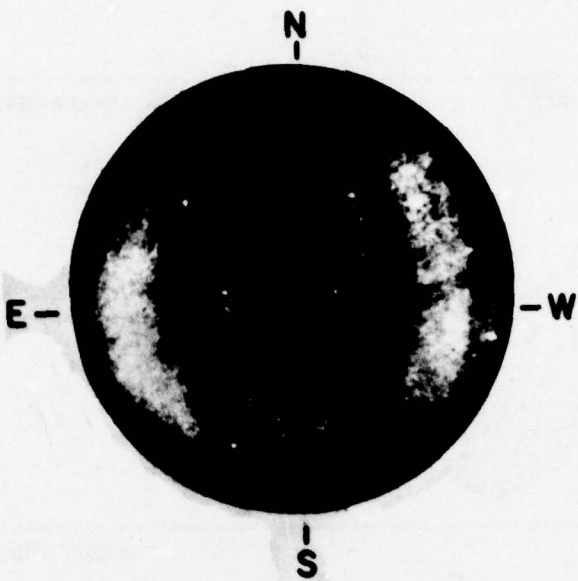


Figure 7.  $6300\text{ \AA}$  All Sky Photometer Image at 0445 UT, 20 March 1977 With Four Well-developed Airglow Depletions

in the Peru sector. The location of the east and west edges of all the depletions observed throughout this flight were determined from the photometer images and are shown in Figure 8 together with the aircraft flight track. The figure clearly shows the eastward drift of the depletions early in the evening, with a gradual decrease and eventual cessation of eastward drift by local midnight. There is also a tendency, on this day, for depletions observed early in the evening (I and II) to be considerably wider than those observed near midnight (III-VII).

The time history of the F-layer virtual height ( $h'F$ ), determined from the aircraft ionograms, is shown in the lower panel of Figure 8 to illustrate F-layer height variations associated with the airglow depletions. An increase in the layer height occurs as the aircraft passes under depletion I, II, III and V. These height increases are 25 to 40 km, approximately the same as that observed for the isolated depletion discussed in Section 3 and substantiate the earlier results of Van Zandt and Peterson.<sup>9</sup> The agreement between height variations and depletion regions is not perfect, however, and this may be related to the inherent difficulty of ionosondes to detect narrow electron density troughs or depletions (Lobb and Titheridge<sup>10</sup>).

---

10. Lobb, R.J., and Titheridge, J.E. (1977) The effect of travelling ionospheric disturbances on ionograms, J. Atmos. Terr. Phys. 39:129.

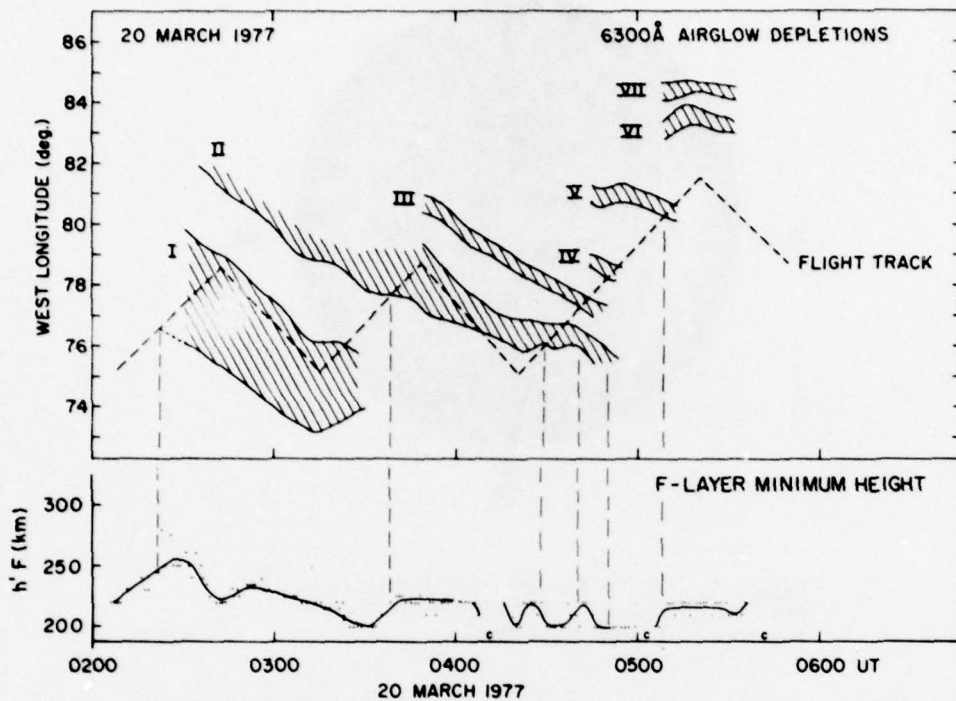


Figure 8. Ground Projection of the East and West Edges of Airglow Depletions Observed During the Flight of 20 March 1977 to Illustrate the Eastward Drift, and the F-layer Virtual Height Changes Associated With the Depletions

##### 5. AIRGLOW DEPLETIONS AT ASCENSION ISLAND

The airglow measurements discussed thus far were made within a few degrees of the magnetic equator near Lima, Peru to achieve close coordination with the Jicamarca radar. As previously discussed, a primary objective was to measure airglow signatures associated with the plasma depletions or plumes. The plumes are thought to arise from a Rayleigh-Taylor type instability (Kelley et al.,<sup>11</sup> and references therein) which depends on a steep bottomside vertical density gradient and a minimum altitude of the F2 peak (Ossakow et al.<sup>12</sup>). These initial conditions

- 11. Kelley, M.C., Haerendel, G., Kappler, H., Valenzuela, A., Balsley, B.B., Carter, D.A., Ecklund, W.L., Carlson, C.W., Häusler, B., and Torbert, R. (1976) Evidence for a Rayleigh-Taylor type instability and upwelling of depleted density regions during equatorial spread F, *Geophys. Res. Letters* 3:448.
- 12. Ossakow, S.L., Zalesak, S.T., McDonald, B.E., and Chaturvedi, P.K. (1979) Nonlinear equatorial spread F: dependence on altitude of the F peak and bottomside background electron density gradient scale length, *J. Geophys. Res.* 84:17.

lead to a positive growth rate for the instability (Scannapieco and Ossakow<sup>13</sup>) which can then be initiated by naturally occurring electron density perturbations. Because of the decreased volume emission rate of 6300 Å ( $O(^1D)$ ) at high altitudes (determined by the molecular oxygen profile), the minimum F-layer height required for plume formation also leads to very low airglow intensities. Thus, it is highly unlikely that the development of plumes after sunset will be observed through 6300 Å airglow near the magnetic equator.

During March 1977 and March 1978, the AFGL Airborne Ionospheric Observatory made 15 flights at equatorial latitudes beginning at sunset. On none of these occasions was the actual formation of a depletion observed in the ambient airglow layer. Rather, when the post-sunset ionosphere decreased in height ( $h'F \leq 275$  km), airglow intensities increased above the all sky photometer detection threshold ( $\sim 25R$ ), and fully developed depletions became visible as dark bands in the ambient airglow. On several occasions, the F-layer height remained above 75 km for the entire night, and no airglow depletions were visible, even though plumes and scintillations were observed.

On 10/11 March 1978, a flight from Ascension Island ( $7.9^{\circ}$ S,  $14.4^{\circ}$ W,  $18^{\circ}$ S Magnetic Latitude) designed to investigate the southern (poleward) extent of ionospheric irregularities, and longitudinal variations (Basu et al<sup>14</sup>) in the km-size irregularities provided considerable new information on the morphology of airglow depletions. The 6300 Å images for this flight, at 10 min intervals, are shown in Figure 9. All images have been reoriented with magnetic north at the top and east to the left. The flight track in Figure 10 shows the aircraft position and flight direction in both geographic and magnetic coordinates for comparison with the images in Figure 9. These measurements were made at higher magnetic latitudes than those in the Peru sector and show several important features. The images from 2100 to 2150 UT show the equatorward edge of the east-west aligned intertropical arc or airglow enhancement associated with the Appleton anomaly. This edge is visible as early as 2020 UT; however, this image also shows some twilight enhancement to the west. Airglow depletions, presumed to be an extension of the same phenomenon measured at the equator, extend into the intertropical arc. The most southerly images at 0000 to 0020 UT show airglow depletions which extend completely through and reach to the poleward edge of the arc.

The depletions are approximately aligned along magnetic meridians. The alignment of airglow depletions may be important in understanding the development phase of bubbles or plumes. Previous measurements have been unable to

---

13. Scannapieco, A.J., and Ossakow, S.L. (1976) Non-linear equatorial spread F, *Geophys. Res. Letters* 3:451
14. Basu, S., Basu, S., and Kahn, B.K. (1976) Model of equatorial scintillations, for in situ measurements, *Radio Sci.* 11:821.

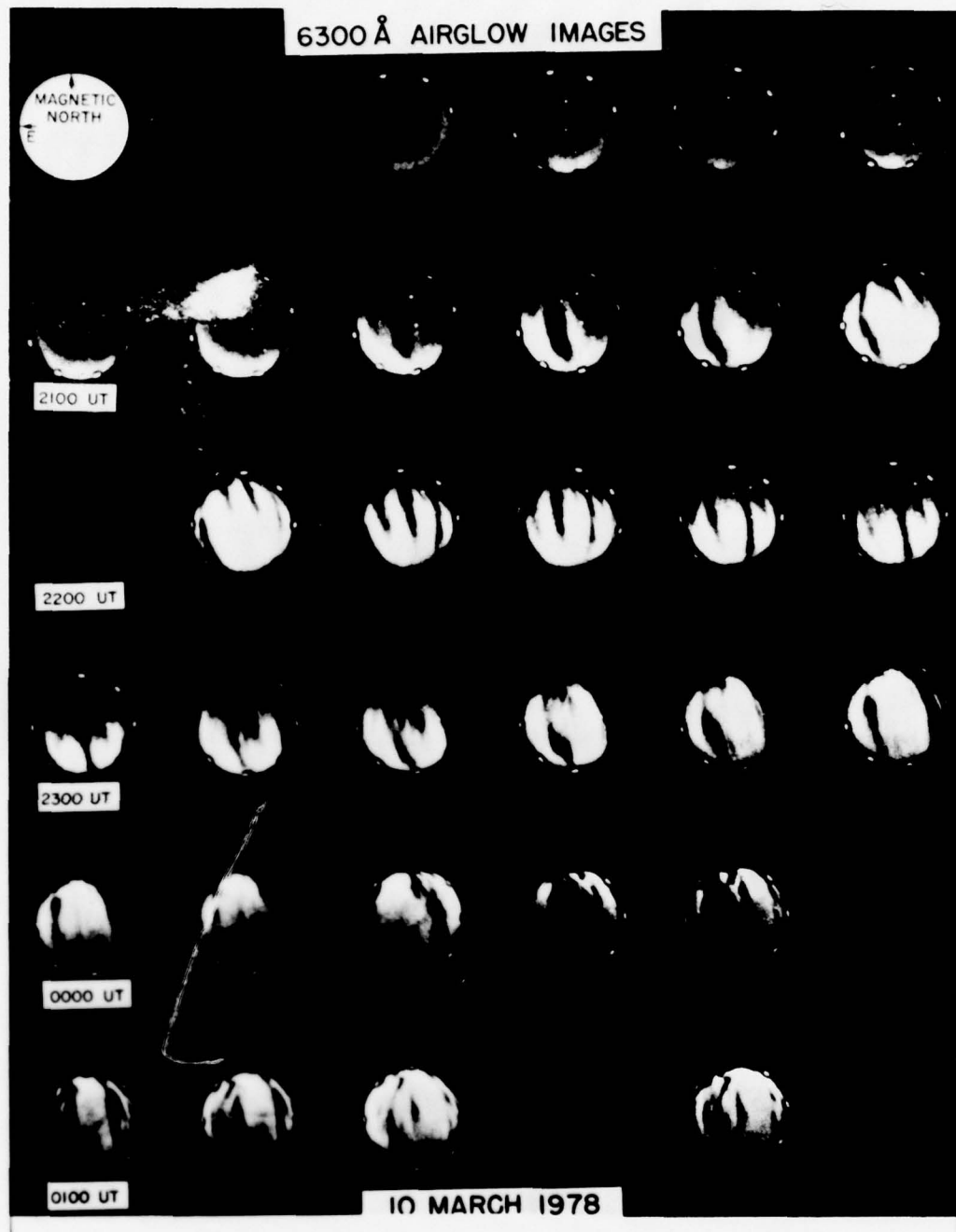


Figure 9. All Sky 6300 Å OI Airglow Images at 10 min Intervals From 2020 to 0140 UT, 10/11 March 1978

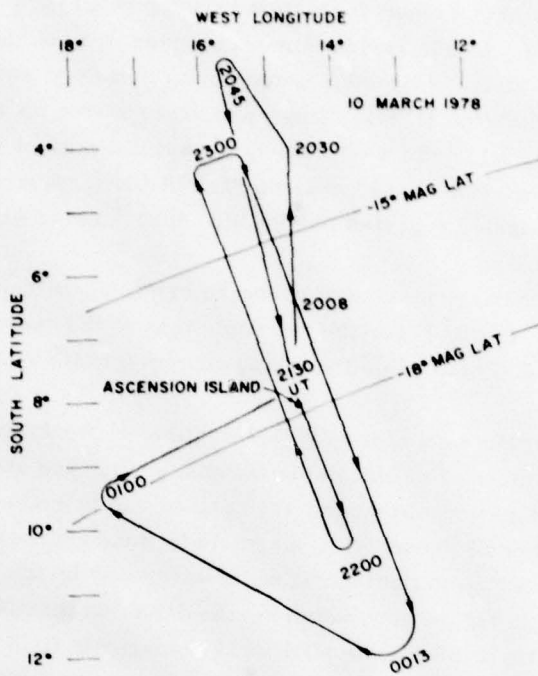


Figure 10. Ground Track for the Flight of  
10/11 March 1978

accurately determine alignment because of insufficient spatial resolution (conventional photometers) or because the observing technique measured only the east-west horizontal dimension at a fixed latitude (incoherent radar, satellite and rocket detectors). Theoretical studies (Ossakow et al<sup>12</sup>; Scannapieco and Ossakow<sup>13</sup>) and models (Woodman and La Hoz<sup>3</sup>) consider plume development only in the east-west and vertical dimensions. After a plume has developed, it is reasonable to assume alignment along magnetic field lines in the absence of electric fields, and the photometric images confirm this alignment. During the initial development phase, however, alignment may depend on the nature of the bottom-side electron density fluctuation or perturbation which initiates the instability. If the perturbation is the result of a natural gravity wave and the associated Traveling Ionospheric Disturbance, the perturbation may be aligned with the terminator. Also, ionospheric electric fields may result in alignment other than along magnetic field lines (McClure et al<sup>15</sup>). Because of the large magnetic declination at

15. McClure, J. P., Hanson, W. B., and Hoffman, J. H. (1977) Plasma bubbles and irregularities in the equatorial ionosphere, *J. Geophys. Res.* 82:2650.

Ascension Island ( $20^{\circ}$ W), a clear distinction between geographic and magnetic alignment is possible. In this region, the photometer images show alignment along magnetic field lines. Alignment determination in Peru was more difficult due to the small declination ( $1^{\circ}$ E). There are cases where the poleward ends of the depletions curve toward the west (depletion west of zenith at 0020 UT). This may be the optical manifestation of the "westward" drift (with respect to the background plasma) of plasma bubbles reported by McClure et al<sup>15</sup> using Atmospheric Explorer ion drift measurements.

Variations occur in the maximum poleward extent of the depletions as seen in the 2210 UT image. In this case, the two depletions in the center of the image terminate at  $\sim 18^{\circ}$  M. Lat., while the single depletion to the east extends to  $\sim 24^{\circ}$  M. Lat.

We propose that the ends of the airglow depletions represent the lower altitude ( $\sim 250$  km) termination of plasma depletions, or bubbles and that through the use of a suitable magnetic field model, the bubbles can be traced to lower magnetic latitudes and to higher altitudes. The magnetic latitude reached by the end of the depletion should thus map to the highest altitude reached by the bubble at the magnetic equator. In the present example, the depletion terminating at  $-18^{\circ}$  M. Lat. traces to 780 km at the equator (IGRF 1975 magnetic field model) and the depletion ending at  $-24^{\circ}$  M. Lat. traces to 1290 km. In this longitude sector, there is presently no means to verify these altitudes. However, they are well within the height of ranges of bubbles observed at Jicamarca (Woodman and La Hoz<sup>3</sup>).

Amplitude scintillations, measured during this period on the aircraft and at Ascension show that the ends of the airglow depletions represent the poleward limit of ionospheric irregularities of kilometer scale size. The magnetic longitude of the east and west edges of airglow depletions observed during the flight are shown in Figure 11. Also shown is the Ascension Island magnetic meridian and the magnetic longitude of the aircraft flight track. The airglow depletions drift from west to east through the aircraft zenith. The amplitude scintillation measurements were made using the MARISAT geostationary satellite which was almost directly overhead (elevation angle  $\geq 85^{\circ}$ ). The lower panel in Figure 11 shows the scintillation index (a measure of the signal fluctuation) for this period, as determined from the airborne satellite data.

Scintillations begin as depletion I drifts over the aircraft, but continue after the western edge has moved to the east of the aircraft. This effect has been reported by Buchau et al<sup>4</sup> and may be related to westward tilts in the topside of the depletion region. Similar effects are observed for depletions III and VI. Note that depletion II which terminated north of the satellite-to-aircraft ray path (see Figure 9) was not associated with a scintillation event.

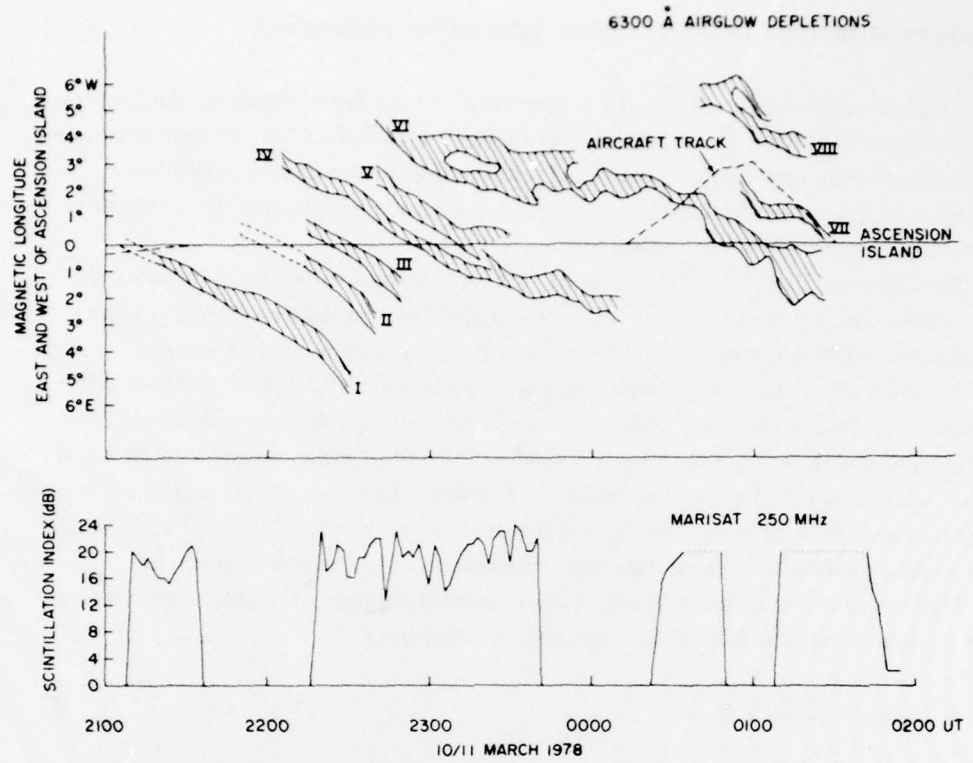


Figure 11. Ground Projection of the East and West Edges of Airglow Depletions Observed During the Flight of 10/11 March 1978, and the 250 MHz Scintillation Index Measured on the Aircraft

Scintillations measured on the ground at Ascension were essentially identical to those measured on the aircraft, except that depletion II, which passed directly over Ascension resulted in a well defined scintillation event (J. Aarons, private communication). Thus, the airglow depletions accurately map the regions containing ionospheric irregularities, and these regions have a sharp boundary (within  $\sim 1.5^\circ$  of latitude) as they map down magnetic field lines from the equator to their low altitude termination. Measurements are planned to investigate this aspect further by simultaneously measuring airglow depletions and scintillations near the low altitude termination of field lines which pass above the Jicamarca radar.

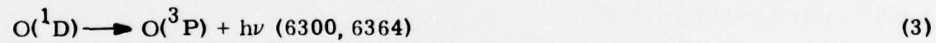
## 6. ELECTRON DENSITY ESTIMATES FROM AIRGLOW MEASUREMENTS

Airglow intensity measurements provide a means for estimating the bottom-side electron density within airglow depletions. Although other remote measurements (ionosonde and VHF backscatter radar) map the location of depletions through associated irregularities, they do not provide a quantitative measure of ionization levels within the depletions.

Through the use of a simple model, airglow measurements can provide a quantitative estimate of the average bottomside electron density structure for comparison with other experimental observations and numerical models.

Airglow intensities were measured on the aircraft with a 1 m Ebert-Fastie scanning spectrometer, and with a narrow band, tilting filter photometer. The spectrometer views the zenith with a  $4.5^\circ \times 5^\circ$  field of view; an area of  $20 \text{ km} \times 20 \text{ km}$  for an assumed emission height of 250 km. Because of the relatively large spectrometer field of view, the tilting filter photometer ( $1.6^\circ$  field of view) was used, when available, to map intensity changes across narrow depletions.

Following the method outlined by Noxon and Johanson,<sup>16</sup> nighttime  $6300\text{\AA}$  airglow results from the following sequence of reactions:



The  $6300\text{\AA}$  volume emission rate is given by:

$$dI(6300) = (0.75 k_1 \epsilon [N_e] [\text{O}_2] / (1 + k_Q [N_2] / A)) dh \quad (5)$$

where  $k_1 \epsilon = 1.4 \times 10^{-11} \text{ cm}^3 \text{ sec}^{-1}$ ,  $k_Q = 7.0 \times 10^{-11} \text{ cm}^3 \text{ sec}^{-1}$ ,  $A = 10^2 \text{ sec}^{-1}$  (see Noxon and Johanson<sup>16</sup> for a more complete discussion). The  $\text{N}_2$  and  $\text{O}_2$

16. Noxon, J. F., and Johanson, A. F. (1970) Effect of magnetically conjugate photoelectrons on OI ( $6300\text{\AA}$ ), Planet. and Space Sci. 18:1367.

concentrations are obtained from the 1977 Jacchia<sup>17</sup> model atmosphere. The measured 6300 Å column emission is then given by:

$$I(6300) = \int_{h_1}^{h_2} dI dh . \quad (6)$$

According to Markham et al.<sup>18</sup> variations in 6300 Å intensity over  $\pm 15^\circ$  of latitude near the magnetic equator are due to changes in the electron concentration, and not to variations in the atmospheric molecular concentration. For the present work, we assume that all of the 6300 Å emission is produced in the altitude range from 350 km down to the base height of the F-layer,  $h'F$ , measured by the aircraft ionosonde, and that spatial variations in the airglow are due to spatial variations in the electron concentration within the same altitude range. This altitude range is appropriate, since above 350 km, the decreased concentration of O<sub>2</sub> leads to decreased emission, and below  $h'F$  (220 km minimum measured) quenching of O(D) by N<sub>2</sub> becomes important. Also, the equatorial ionosphere exhibits a steep bottomside gradient in the evening (Farley et al<sup>19</sup>) and the electron concentration below  $h'F$  is greatly diminished. In regions where O<sup>+</sup> is the dominant ion (above  $\sim 210$  km), [O<sup>+</sup>] = [Ne] and the steep bottomside gradient in O<sup>+</sup> leads to decreased production of O(D) below  $h'F$  through reactions (1) and (2). As an approximation, the measured virtual base height,  $h'F$ , has been used as the true base height,  $h_{min} F$ , since spread F conditions and the 2 MHz low frequency cutoff of the airborne ionosonde prevent determination of the actual base height through true height analysis. Because of the steep bottomside gradient, however, substitution of  $h'F$  for  $h_{min} F$  results in only a small error.

To derive the average electron density over the height range  $h'F$  to 350 km, we replace [Ne] in equation (5) by an average electron density,  $\langle Ne \rangle$ , which does not vary over this altitude range. Here  $\langle Ne \rangle$  is defined as:

$$\langle Ne \rangle = \frac{\int_{h'F}^{350} [Ne] dh}{(350 - h'F)} \quad (7)$$

---

- 17. Jacchia, L. G. (1977) Thermospheric temperature, density and composition New models, Smithson. Astrophys. Observ. Spec. Rept. 375.
- 18. Markham, T. P., Buchau, J., Anctil, R. E., and Noxon, J. F. (1965) Airborne study of equatorial 6300 Å nightglow, J. Atmos. and Terrestrial Phys. 37:65.
- 19. Farley, D. T., Balsley, B. B., Woodman, R. F., and McClure, J. P. (1970) Equatorial spread F: implications of VHF radar observations, J. Geophys. Res. 75:7199.

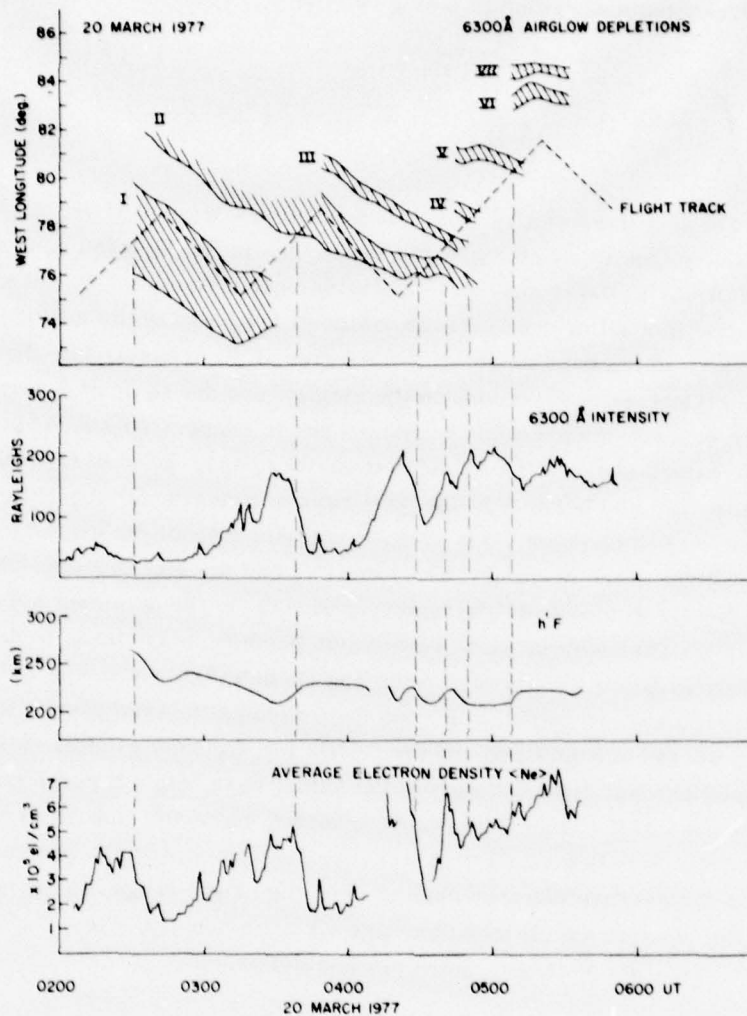


Figure 12. Ground Projection of the Airglow Depletions,  $6300 \text{ \AA}$  Zenith Intensity, F-layer Virtual Height and Calculated Average Bottomside Electron Density for the Flight of 20 March 1977

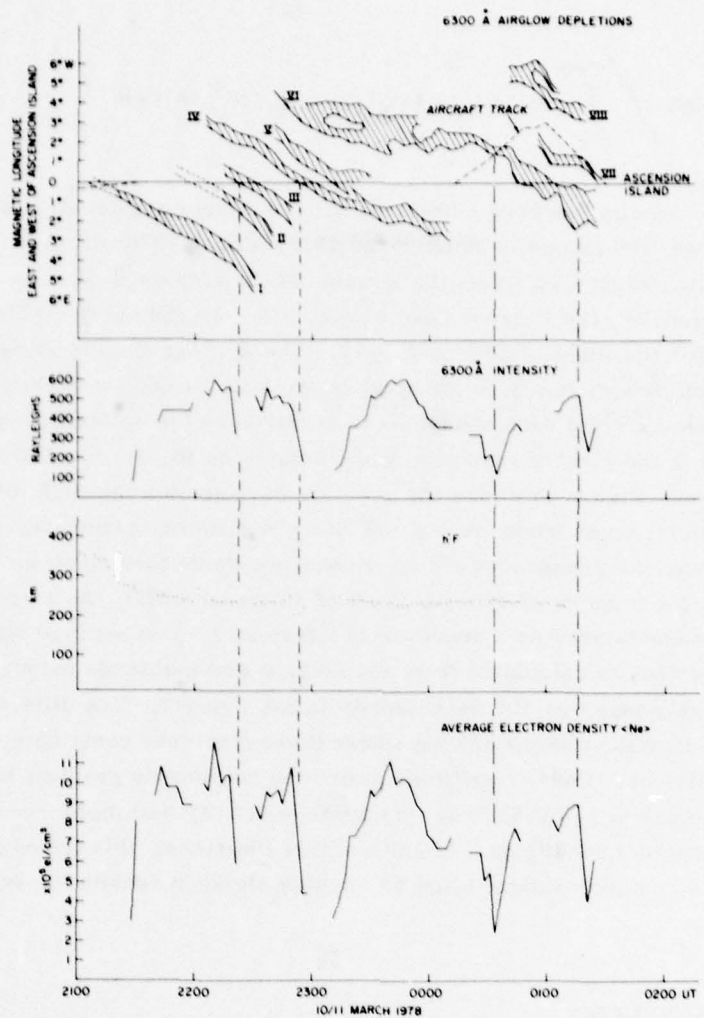


Figure 13. Ground Projection of the Airglow Depletions, 6300 Å Zenith Intensity, F-layer Virtual Height and Calculated Average Bottomside Electron Density for the Flight of 10/11 March 1977

The average electron density is then related to the measured  $6300\text{ \AA}$  intensity through:

$$\langle Ne \rangle = I(6300) \int_{h'F}^{350} (0.75 k_1 e [O_2] / (1 + k_Q [N_2] / A)) dh \quad (8)$$

The average density has been calculated for two flights previously discussed 20 March 1977 near the magnetic equator and 10/11 March 1978 within the Appleton anomaly. Figure 12 shows the location of the airglow depletions, the zenith  $6300\text{ \AA}$  intensity, the F-layer base height,  $h'F$ , and the calculated average density,  $\langle Ne \rangle$ , for the flight of 20 March 1977. The average density varies by a factor of  $\sim 3$  from outside to inside the airglow depletions ( $\sim 66$  percent depletion), provided the depletions are wide enough to be resolved by the optical measurements. Depletions I and II are clearly resolved, while depletions III, IV and V are only partially resolved. Figure 13 shows the same parameters for the flight of 10/11 March 1978, which ranged from  $-12^\circ$  to  $-22^\circ$  magnetic latitude within the Appleton anomaly. Although the background electron density outside the depletions is much larger on this flight (compared with the flight of 20 March 1977), the airglow depletions are still characterized by a decrease of a factor of  $\sim 3$  in average density.

The average density calculated from the airglow and ionosonde measurements can be considerably less than the peak density in the F-layer. The difference arises when the F peak is above 350 km where these electrons contribute very little to the  $6300\text{ \AA}$  emission. Under conditions where the bottomside gradient is very steep and the F-peak is below 350 km, the average density will more closely approximate the actual conditions. In spite of this limitation, this technique provides a means to remotely estimate the bottomside electron density for extended periods.

## 7. NORTH-SOUTH SYMMETRY

A flight from Ascension ( $7.98^\circ S$ ,  $14.42^\circ W$ ,  $-18^\circ$  M. Lat.) to Zanderij, Surinam ( $5.45^\circ N$ ,  $55.18^\circ W$ ,  $+15^\circ$  M. Lat.) on 12 March 1978 provided the opportunity to observe ionospheric and airglow structures north and south of the magnetic equator within a 5 hr period.

The two images shown in Figure 14 summarize the main result from this flight: airglow depletions are symmetric about the magnetic equator. The figure shows images made north and south of the magnetic equator. The image at 2245 UT shows

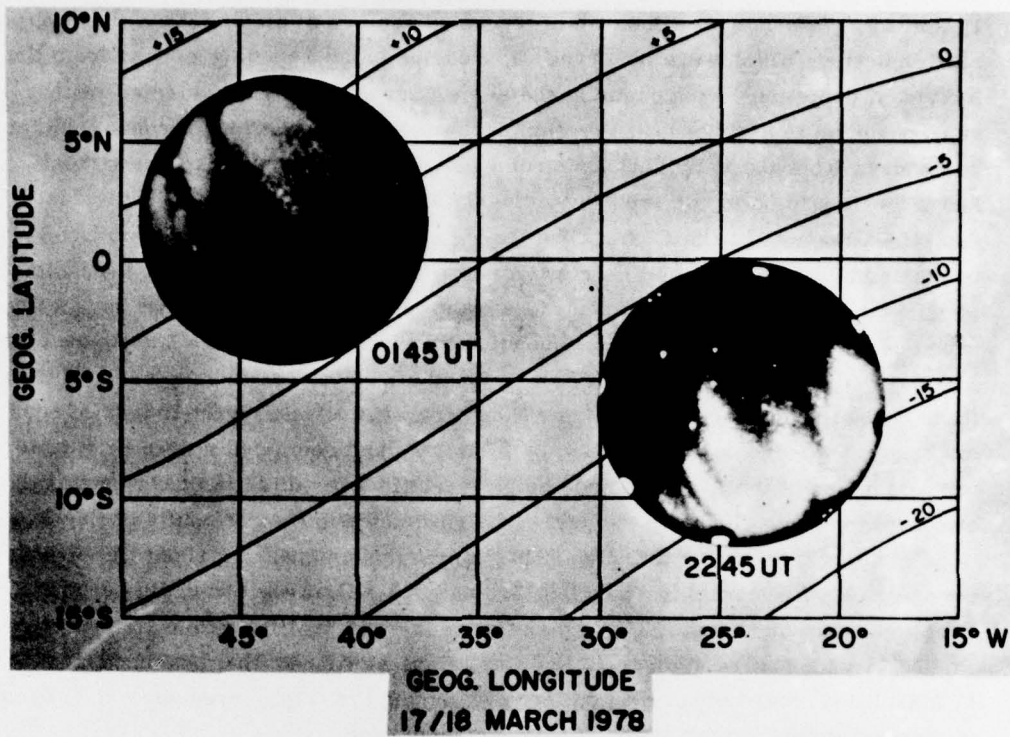


Figure 14.  $6300\text{\AA}$  Airglow Images North and South of the Magnetic Equator on 12 March 1978

airglow depletions within the southern intertropical arc extending toward the equator. Airglow intensities fall below the detection limit by  $-12^\circ$  to  $-10^\circ$  M. Lat., due to the increase in altitude of the F-region toward the equator. The airglow structures in the 0145 UT image are essentially the reverse of those in the 2245 UT image; airglow depletions are present within the northern intertropical arc and extend toward the equator. Thin clouds were present above the aircraft at 0145 UT which make the airglow structures less distinct, although the overall pattern is evident. Amplitude scintillation measurements made on the aircraft show that ionospheric irregularities, resulting in UHF amplitude scintillations between 25 and 30 dB were present above the aircraft throughout the period 2245 to 0145 UT.

Ionomsonde measurements made throughout the flight show the existence of bottomside electron density depletions across the entire observation region from  $14^\circ$  South to over  $12^\circ$  North magnetic latitude. The existence of these structures, which were similar to the isolated bottomside depletion observed on 17 March 1977 (described in section 3.2 and Figure 5), could easily be observed on the time-lapse

16 mm ionogram movie. Because of the large number of airglow, and thus bottom-side depletions which were observed, approaching and receding echoes from the individual depletions often occur at the same virtual range. Because of these superposed oblique echoes, the motion of the individual scattering fronts could not be deduced from the individual ionograms. A technique which displays virtual range vs time for a single frequency clearly shows the motion of the individual depletions throughout the flight. The three panels in Figure 15 were produced by cutting narrow ( $\sim 100$  KHz) strips from the individual ionograms at the indicated frequencies. The sequence of strips thus shows the virtual height and backscatter range of echoes at the selected frequencies throughout the flight. The figure shows that the F-layer virtual height ( $h'F$ ) was found at  $\sim 240$  km at the beginning of the flight, slowly increased to  $>320$  km as the aircraft approached the magnetic equator, and then decreased to  $\sim 275$  km by  $8^{\circ}$  North, and remained at this height for the remainder of the flight. These height variations resulted in the changes in airglow intensities discussed above. Of significance to the continuity of the depletions are the backscatter branches. In general these appear as echoes approaching the aircraft at the lower frequencies (3.0 and 3.5 MHz); while receding echoes are simultaneously observed at the higher frequencies (5.5 MHz). Comparison of Figure 14 with Figure 4 suggests that depletions similar to that observed on 17 March 1977 were observed continuously during the flight, even when the absence of airglow did not permit their optical documentation.

The structure ranges from a large number of smaller depletions between 2145 and 2330 UT, to fewer, but better defined depletions while crossing the magnetic equator. During the final segment of the flight north of the equator, the traces again show smaller, less well defined structures. From this single flight, however, it is not possible to determine if the suggested change in irregularity structure reflects temporal or latitudinal variations.

The frequency dependence of the backscatter which appears as larger amplitude echoes at lower frequencies for approaching fronts (trailing edge of depletions), and at higher frequencies for receding front (leading edges) may be due to a difference in structure of the two edges as reported by Röttger.<sup>20</sup>

From the relationship between airglow depletions and ionospheric irregularities previously discussed, we infer that ionospheric bubbles or plumes extend continuously across the magnetic equator and involve entire magnetic flux tubes. The low altitude (higher latitude) ends of these plumes are made visible through the associated airglow depletions, while the high altitude (lower latitude) portion can often only be detected with ionosonde, amplitude scintillation, backscatter

---

20. Röttger, J. (1973) Wave-like structures of large scale equatorial spread-F irregularities, *J. Atmos. and Terrestrial Phys.* 35:1195.

**TRANSEQUATORIAL FLIGHT ASCENSION TO SURINAM**  
**12/13 MARCH 1978**

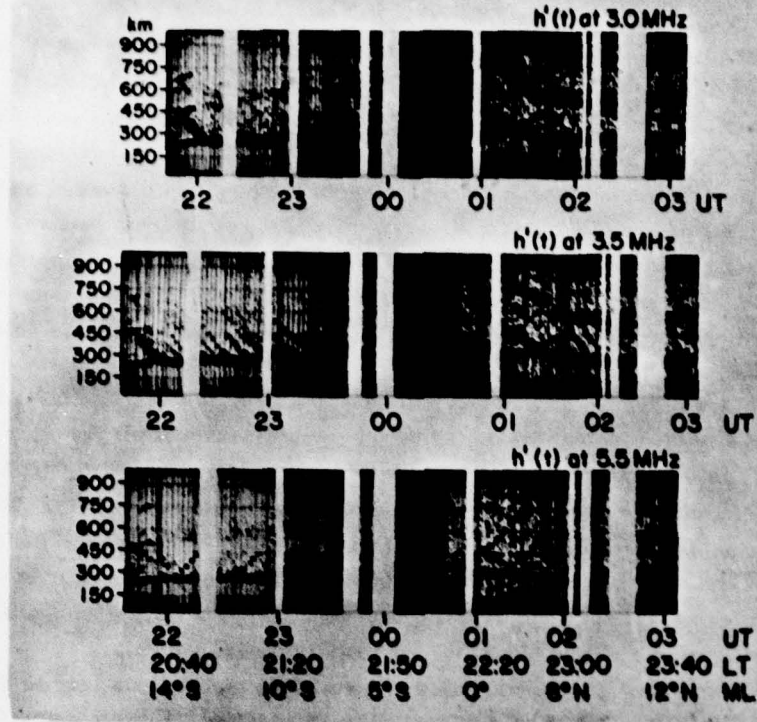


Figure 15. Virtual Range vs. Time Plots at Selected Frequencies to Show Range Changes Associated with Electron Density Depletions

radar and in situ plasma measurements. Dyson and Benson<sup>21</sup> have recently shown the magnetic field alignment of plasma depletions using topside sounder measurements. From the ionogram traces two-dimensional structure along field lines, as well as electron density distributions characterizing the depletions, have been determined.

In a recent paper, Szuszczewicz<sup>22</sup> discussed the need for containment of plasma depletions along the direction of the magnetic field to limit the North-South extent. In view of the airglow measurements presented in this paper, and the sounder measurements of Dyson and Benson,<sup>21</sup> there is no need for containment parallel to the magnetic field, since the depletions extend along the entire flux tube.

---

- 21. Dyson, P. L., and Benson, R. F. (1978) Topsider sounder observations of equatorial bubbles, Geophys. Res. Letters 5:795.
- 22. Szuszczewicz, E. P. (1978) Ionospheric holes and equatorial spread F: chemistry and transport, J. Geophys. Res. 83:2665.

## 8. SUMMARY AND DISCUSSION

From the combined optical and ionospheric measurements conducted as part of the AFGL equatorial scintillation studies, a more complete description of equatorial ionospheric processes has emerged. The optical measurements provide a two-dimensional bottomside view of the ionospheric bubbles or plumes which extend into the topside ionosphere and across the entire equatorial region. The bubbles are regions of low electron and ion density that result from bottomside instabilities which propagate upward through the F-layer peak, often reaching to 1000 km altitude. Within these regions, ionospheric irregularities with scale sizes from 3 m to 10 km give rise to 50 MHz backscatter, VHF amplitude scintillation and spread F.

From combined airglow and ionosonde measurements, the average bottomside electron density has been determined, inside and outside several airglow depletions. The results of these calculations show typical depletions of  $\sim 66$  percent, near the magnetic equator as well as near the southern Appleton anomaly. The magnitude of these depletions agree with the measurements of Dyson and Benson,<sup>21</sup> and Kelley et al<sup>11</sup>; and the numerical simulation of Ossakow et al.<sup>12</sup> They are, however, much less than the large depletions of up to three orders of magnitude reported by McClure et al.,<sup>15</sup> using AE-C ion density measurements.

Current experimental measurements and numerical simulations lead to different descriptions of the structure of the bottomside ionosphere within a depletion region. The picture presented by Dyson and Benson<sup>21</sup> is a depletion with limited vertical thickness. This implies that the bottomside ionosphere is filled-in below the depletion at all latitudes except where the flux tubes containing the depletion map to low altitudes. In the example presented by Dyson and Benson<sup>21</sup> (their Figure 4), the associated airglow depletion would be expected over a limited latitude range of  $\sim 300$  km, where the plasma depletion maps into the bottomside. Measurements presented in this report show that airglow depletions often extend for 3000 km in the North-South direction, implying an absence of bottomside plasma over similar dimensions. From the airglow measurements, we conclude that the bottomside remains depleted of plasma as the top of the depletion rises to high altitudes. Since single airglow depletions have been monitored by aircraft measurements for over two hours, the bottomside remains depleted over a similar time scale.

The numerical simulations of Ossakow et al.,<sup>12</sup> show the absence of bottomside plasma in their examples of plasma density depletion (bubble) formation. In some cases, even after  $\sim 3$  hours, the largest percentage depletion, compared to the background ionosphere, occur below the F peak. Using East-West dimensions of

~100 km in the models (Zalesak et al<sup>23</sup>) which more closely resemble the observed depletions, the electron density profiles from the numerical simulations would produce airglow depletions similar to those observed.

---

23. Zalesak, S. T., Ossakow, S. L., McDonald, B. E., and Chaturvedi, P. K.  
(1978) Spatially large equatorial spread F Bubbles (abstract), EOS Trans.  
AGU 59:345.

## References

1. Weber, E.J., Buchau, J., Eather, R.H., and Mende, S.B. (1978) North-south aligned equatorial airglow depletions, J. Geophys. Res. 83:712.
2. Buchau, J., Weber, E.J., and McClure, J.P. (1978a) Radio and optical diagnostics applied to an isolated equatorial scintillation event, Proc. Ionospheric Effects Symp., Arlington, VA.
3. Woodman, R.F., and LaHoz, C. (1976) Radar observations of F-region equatorial irregularities, J. Geophys. Res. 81:5447.
4. Buchau, J., Weber, E.J., and Whitney, H.E. (1978b) New insight into ionospheric irregularities and associated VHF/UHF scintillations, Proc. AGARD Conf., Digital Communications in Avionics, Munich, Germany.
5. Mende, S.B., Eather, R.H., and Aamodt, E.K. (1977) Instrument for the monochromatic observation of all sky auroral images, Appl. Opt. 16:1691.
6. Barbier, D. (1961) Les variations d'intensité la raie 6300 Å la luminescence nocturne, Ann. Geophys. 17:5.
7. Barbier, D., Weill, G., and Glaume, J. (1961) L'émission de la raie rouge du ciel nocturne en Afrique, Ann. Geophys. 17:305.
8. Steiger, W.R. (1967) Low Latitude Observations of Airglow, in Aurora and Airglow, edited by B.M. McCormac, p. 419, Reinhold, New York.
9. Van Zandt, T.E., and Peterson, V.L. (1968) Detailed maps of tropical 6300 Å nightglow enhancements and their implications on the ionospheric F2 layer, Ann. Geophys. 24:747.
10. Lobb, R.J., and Titheridge, J.E. (1977) The effect of travelling ionospheric disturbances on ionograms, J. Atmos. Terr. Phys. 39:129.
11. Kelley, M.C., Haerendel, G., Kappler, H., Valenzuela, A., Balsley, B.B., Carter, D.A., Ecklund, W.L., Carlson, C.W., Häusler, B., and Torbert, R. (1976) Evidence for a Rayleigh-Taylor type instability and upwelling of depleted density regions during equatorial spread F, Geophys. Res. Letters 3:448.

12. Ossakow, S. L., Zalesak, S. T., McDonald, B. E., and Chaturvedi, P. K. (1979) Nonlinear equatorial spread F: Dependence on altitude of the F peak and bottomside background electron density gradient scale length, *J. Geophys. Res.* 84:17.
13. Scannapieco, A. J., and Ossakow, S. L. (1976) Non-linear equatorial spread F, *Geophys. Res. Letters* 3:451.
14. Basu, S., Basu, S., and Kahn, B. K. (1976) Model of equatorial scintillations, for *in situ* measurements, *Radio Sci.* 11:821.
15. McClure, J. P., Hanson, W. B., and Hoffman, J. H. (1977) Plasma bubbles and irregularities in the equatorial ionosphere, *J. Geophys. Res.* 82:2650.
16. Noxon, J. F., and Johanson, A. F. (1970) Effect of magnetically conjugate photoelectrons on OI (6300 Å), *Planet. and Space Sci.* 18:1367.
17. Jacchia, L. G. (1977) Thermospheric temperature, density and composition: New models, *Smithson. Astrophys. Observ. Spec. Rept.* 375.
18. Markham, T. P., Buchau, J., Anctil, R. E., and Noxon, J. F. (1965) Airborne study of equatorial 6300 Å nightglow, *J. Atmos. and Terrestrial Phys.* 37:65.
19. Farley, D. T., Balsley, B. B., Woodman, R. F., and McClure, J. P. (1970) Equatorial spread F: implications of VHF radar observations, *J. Geophys. Res.* 75:7199.
20. Röttger, J. (1973) Wave-like structures of large scale equatorial spread-F irregularities, *J. Atmos. and Terrestrial Phys.* 35:1195.
21. Dyson, P. L., and Benson, R. F. (1978) Topside sounder observations of equatorial bubbles, *Geophys. Res. Letters* 5:795.
22. Szuszczewicz, E. P. (1978) Ionospheric holes and equatorial spread F: chemistry and transport, *J. Geophys. Res.* 83:2665.
23. Zalesak, S. T., Ossakow, S. L., McDonald, B. E., and Chaturvedi, P. K. (1978) Spatially large equatorial spread F bubbles (abstract) *EOS Trans. AGU* 59:345.

## DISTRIBUTION LIST

### Department of Defense

Assistant Secretary of Defense Comm, Cmd, Cont & Intell Attn: C31 ST&CCS M Epstein Attn: J Babcock	Director Defense Nuclear Agency 3cy Attn: RAAE Attn: DDST 4cy Attn: TITL Attn: SIVL
Assistant to the Secretary of Defense Atomic Energy Attn: Executive Assistant	Commander Field Command Defense Nuclear Agency Attn: FCPR
Director Command Control and Technical Center Attn: C-650 G Jones Attn: C-650 W Heidig Attn: C-312 R Mason	Chief Field Command Defense Nuclear Agency Livermore Division Attn: FCPRL
Director Defense Advanced Res Proj Agency Attn: TIO	Director Interservice Nuclear Weapons School Attn: TTV
Director Defense Communications Agency Attn: Code 205 Attn: Code 480 Attn: Code 810 J Barna Attn: Code 101B Attn: Code R1033 M Raffensperger	Joint Chiefs of Staff Attn: J-3 WWMCCS Evaluation Office Attn: J-37
Defense Communications Engineer Center Attn: Code R123 (Tech Lib) Attn: Code R410 J McLean Attn: Code R720 J Worthington	Director Joint Strat Tgt Planning Staff Attn: JLTW-2 Attn: JPST G Goetz
Defense Documentation Center 12cy Attn: DD	Director National Security Agency Attn: W32 D Bartlett Attn: R52 J Skillman Attn: B3 F Leonard
Director Defense Intelligence Agency Attn: DC-7D W Wittig Attn: HQ-TR J Stewart Attn: DB-4C E O'Farrell Attn: DT-1BZ R Morton Attn: DB A Wise Attn: DT-5 Attn: DT-1B	Under Secy of Def for Rsch & Engrg Department of Defense Attn: Strategic and Space Systems (OS)
	WWMCCS System Engineering Org Attn: R Crawford

Department of the Army

Commander/Director  
Atmospheric Sciences Laboratory  
U S Army Electronics R&D Command  
Attn: DELAS-EO F Niles

Commander  
BDM Systems Command  
Department of the Army  
2cy Attn: BMDSC-HW

Deputy Chief of Staff for Ops & Plans  
Department of the Army  
Attn: DAMO-TCW  
Attn: DAMO-TCZ P Kenny

Commander  
Electronics Tech and Devices Lab  
U S Army Electronics R & D Command  
Attn: DELET-ER H Bomke

Commander  
Harry Diamond Laboratories  
Department of the Army  
Attn: DELHD-I-TL M Weiner  
Attn: DELHD-N-P  
Attn: DELHD-N-RB R Williams  
Attn: DELHD-N-P F Wimenitz

Commander  
U S Army Comm-Elec Engrg Instal Agency  
Attn: CCC-EMEO-PED G Lane  
Attn: CCC-EMEO W Nair

Commander  
U S Army Communications Command  
Attn: CC-OPS-WR H Wilson

Commander  
U S Army Foreign Science & Tech Ctr  
Attn: DRXST-SD

Commander  
U S Army Materiel Dev & Readiness Cmd  
Attn: DRCLDC J Bender

Commander  
U S Army Nuclear & Chemical Agency  
Attn: Library

Commander  
U S Army Satellite Comm Agency  
Attn: Document Control

Director  
U S Army TRADDC Systems Analysis Activity  
Attn: ATAA-PL  
Attn: ATAA-TDC  
Attn: ATAA-TCC F Payan JUNIOR

Department of the Navy

Director  
Joint Cruise Missile Project Office  
Attn: JCM-G-70

Commander  
Air Naval Development Center  
Attn: Code 6091 M Setz

Commander  
Naval Electronics Systems Command  
Attn: PME 117-T  
Attn: Code 501A  
Attn: PME 117  
Attn: PME 106-13 T Griffin  
Attn: PME 106-4 S Kkearney  
Attn: NAVELEX-3101 T Hughes

Commanding Officer  
Naval Intelligence Support Ctr  
Attn: NISC-50

Commander  
Naval Oceans Systems Center  
3cy Attn: Code 5324 W Moler  
Attn: Code 8151 C Baggett  
Attn: M Paulson

Commanding Officer  
Nava Research Laboratory  
Attn: Code 6707 J Davis  
Attn: Code 6701 J Brown  
Attn: Code 7580  
Attn: Code 7555  
Attn: Code 7500 B Wald  
Attn: Code 6700 T Coffey

Commanding Officer Naval Space Surveillance System Attn: J Burton	Air Force Geophysics Laboratory Attn: OPR-1 J Ulwick Attn: PHP J Aarons Attn: LKB K Champion Attn: OPR A Stair Attn: PHI J Buchau Attn: PHP J Mullen
Officer in Charge Naval Surface Weapons Center White Oak Laboratory Attn: Code F31	Air Force Weapons Laboratory Attn: SUL Attn: DYC
Commander Naval Surface Weapons Center Attn: Code F-14 R Butler	Commander Air Logistics Command Attn: OD-ALC/MM R Blackburn
Commander Naval Telecommunications Command Attn: Code 341	Assistant Chief of Staff Intelligence Attn: INED
Office of Naval Research Attn: Code 420 Attn: Code 421	Assistant Chief of Staff Studies & Analyses Attn: AF/SASC Attn: AF/SASC R Paul
Office of the Chief of Naval Operations Attn: OP 604 Attn: OP 981N Attn: OP 941D	Deputy Chief of Staff Operations Plans and Readiness Attn: AFXOKT Attn: AFXOKCD Attn: AFXOXFD
Director Strategic Systems Project Office Department of the Navy Attn: NSSP-2722 F Wimberly Attn: NSP-43 (Tech Lib) Attn: NSP-2141	Deputy Chief of Staff Research, Development, & Acq Attn: AFRDSP Attn: AFRDQ Attn: AFRDSS Attn: AFRDS
<u>Department of the Air Force</u>	Headquarters Electronic Systems Division Attn: DCKC J Clark Attn: XRW J Deas Attn: YSEA Attn: YSM J Kobelski
Commander Aerospace Defense Command/DC Department of the Air Force Attn: DC MR Long	Commander Foreign Technology Division, AFSC Attn: NIIS Library Attn: TQTD B Ballard
Commander Aerospace Defense Command/XPD Attn: XP Attn: XPDQ	
Air Force Avionics Laboratory Attn: AAD W Hunt Attn: AAD A Johnson	

<u>Commander</u>	<u>Department of Defense Contractors</u>
Rome Air Development Center, AFSC	Aerospace Corp
Attn: ISLD	Attn: N Stockwell
Attn: OCS V Coyne	Attn: I Garfunkel
Attn: EEP	Attn: D Olsen
Space and Missile Systems Organization	Attn: S Bower
Attn: MNNL S Kennedy	Attn: J Carter
Attn: SKA C Rightmyer	Attn: R Slaughter
Attn: SKA M Clavin	Attn: F Morse
Attn: SZJ L Doan	Attn: T Salmi
Attn: V Josephson	
Strategic Air Command/XFSS	Alaska, University of Geophysical Institute
Attn: DCX	Attn: T Davis
Attn: NRT	Attn: N Brown
Attn: OOKSN	Attn: Technical Library
Attn: DCXF	
Attn: XFSS	
Attn: DCXT	
<u>Other Government</u>	Analytical Systems Engineering Corp
Central Intelligence Agency	Attn: Radio Sciences
Attn: OSI/PSTD	
Department of Commerce	Barry Research Communications
National Bureau of Standards	Attn: J McLaughlin
Attn: R Moore	
Department of Commerce	Bow Corp
National Oceanic & Atmos Admin	Attn: L Jacobs
Environmental Research Laboratories	
Attn: R Grubb	Berkeley Research Associates, Inc
Attn: Aeronomy Lab G Reid	Attn: J Workman
Institute for Telecommunication Sci	Boeing Co
National Telecomm & Info Admin	Attn: J Kenney
Attn: A Jean	Attn: D Murray
Attn: L Berry	Attn: G Hall
Attn: D Crombie	Attn: S Tashird
Attn: W Utlauf	
Commandant	Calif at San Diego, University of
U S Coast Guard	IPAPS, B-019
Department of Transportation	Attn: H Booker
Attn: G-DOE-3/TP54 B Romine	
	Charles Stark Draper Lab, Inc
	Attn: J Gilmore
	Attn: D Cox
	Computer Sciences Corp
	Attn: H Blank

Comsat Labs  
Attn: G Hyde  
Attn: R Taur

Cornell University  
Dept of Electrical Engineering  
Attn: D Farley

Electrospace Systems, Inc  
Attn: H Logston

ESL, Inc  
Attn: C Prettie  
Attn: J Roberts  
Attn: J Marshall

Ford Aerospace & Communications Corp  
Attn: J Mattingley

General Electric Co  
Space Division  
Attn: M Bortner

General Electric Co  
Attn: F Reibert

General Electric Co-TEMPO  
Attn: T Stevens  
Attn: M Stanton  
Attn: DASIAC  
Attn: D Chandler  
Attn: W Knapp

General Electric Tech Services Co, Inc  
Attn: G Millman

General Research Corp  
Santa Barbara Division  
Attn: J Ise  
Attn: J Garbarino

GTE Sylvania, Inc  
Electronics Systems Grp-Eastern Div  
Attn: M Cross

HSS, Inc  
Attn: D Hansen

IBM Corp  
Attn: F Ricci

Illinois, University of  
Attn: K Yeh

Institute for Defense Analysis  
Attn: J Bengston  
Attn: J Aein  
Attn: H Wolfhard  
Attn: E Bauer

International Tel & Telegraph Corp  
Attn: Technical Library

JAYCOR  
Attn: S Goldman

Johns Hopkins University  
Applied Physics Lab  
Attn: P Komiske  
Attn: J Newland  
Attn: T Potemra  
Attn: Document Librarian  
Attn: T Evans  
Attn: B Wise

Kaman Sciences Corp  
Attn: T Meagher

Lawrence Livermore Laboratory  
University of California  
Attn: Doc Con for Tech Info Dept

Linkabit Corp  
Attn: I Jacobs

Litton Systems, Inc  
AMECOM Div  
Attn: R Grasty

Lockheed Missiles and Space Co, Inc  
Attn: D Churchill  
Attn: Dept 60-12

Lockheed Missiles and Space Co, Inc  
Attn: R Johnson  
Attn: W Imhof  
Attn: M Walt

Los Alamos Scientific Laboratory  
Attn: Doc Con for R Taschek  
Attn: D Westervelt  
Attn: P Keaton

<b>M.I.T. Lincoln Lab</b>	RAND Corp
Attn: L Loughlin	Attn: C Crain
Attn: D Towle	Attn: E Bedrozian
<b>McDonnell Douglas Corp</b>	Riverside Research Institute
Attn: W Olson	Attn: V Trapani
Attn: J Moule	
Attn: G Mroz	
Attn: N Harris	
<b>Mission Research Corp</b>	Rockwell International Corp
Attn: R Hendrick	Collins Telecomm Sys Div
Attn: D Sowle	Attn: J Kristof
Attn: F Fajen	
Attn: S Gutsche	
Attn: R Bogusch	
Attn: M Scheibe	
<b>MITRE Corp</b>	SANDIA Laboratories
Attn: G Harding	Livermore Laboratory
Attn: A Kymmel	Attn: Doc Con for B Murphrey
Attn: C Callahan	Attn: T Cook
<b>MITRE Corp</b>	SANDIA Laboratories
<b>Westgate Research Park</b>	Attn: Doc Con for ORG 1250 W Brown
Attn: W Hall	Attn: D Thornbrough
Attn: W Foster	Attn: Space Proj Div
Attn: M Horrocks	Attn: D Dahlgren
	Attn: 3141
<b>Pacific-Sierra Research Corp</b>	Science Applications, Inc
Attn: E Field	Attn: L Linson
<b>Penn State University</b>	Attn: C Smith
<b>Ionosphere Research Lab</b>	Attn: J McDougall
Attn: Ionosphere Res Lab	Attn: D Hamlin
<b>Photometrics, Inc</b>	Attn: D Sachs
Attn: I Kofsky	Attn: E Straker
<b>Physical Dynamics, Inc</b>	Science Applications, Inc
Attn: E Fremouw	Attn: D Divis
<b>R &amp; D Associates</b>	Science Applications, Inc
Attn: W Karzas	Attn: SZ
Attn: H Ory	
Attn: C Greifinger	
Attn: F Gilmore	
Attn: R Turco	
Attn: M Gantsweg	
Attn: W Wright	
Attn: R Lelevier	
Attn: B Gabbard	
Attn: C MacDonald	
	SRI International
	Attn: R Leadabrand
	Attn: W Chesnut
	Attn: M Baron
	Attn: C Rino
	Attn: R Livingston
	Attn: W Jaye
	Attn: D Neilson
	Attn: G Price
	Attn: G Carpenter
	Attn: A Burns
	Attn: G Smith

**Teledyne Brown Engineering**  
Attn: R Deliberis

**TRI-COM, Inc**  
Attn: D Murray

**TRW Defense & Space Sys Group**  
Attn: R Plebuch  
Attn: S Altschuler  
Attn: D Dee

**Utah State University**  
**Space Measurements Lab**  
Attn: K Baker  
Attn: L Jensen

**Visidyne, Inc**  
Attn: J Carpenter